Repulsive Λ potentials in dense neutron star matter and binding energy of Λ in hypernuclei

Asanosuke Jinno,[1] Koichi Murase,[2] Yasushi Nara,[3] and Akira Ohnishi[2,*]
[1]*Department of Physics, Faculty of Science, Kyoto University, Kyoto 606-8502, Japan*
[2]*Yukawa Institute for Theoretical Physics, Kyoto University, Kyoto 606-8502, Japan*
[3]*Akita International University, Yuwa, Akita-city 010-1292, Japan*

(Received 14 July 2023; accepted 9 November 2023; published 12 December 2023)

The repulsive three-body force between the lambda (Λ) hyperon and medium nucleons is a key element in solving the hyperon puzzle in neutron stars. We investigate the binding energies of the Λ hyperon in hypernuclei to verify the repulsive Λ potentials from the chiral effective field theory (χEFT) employing the Skyrme Hartree-Fock method. We find that the χEFT Λ potential with Λ*NNN* three-body forces reproduces the existing hypernuclear binding energy data, whereas the Λ binding energies are overestimated without the Λ*NNN* three-body force. Additionally, we search for the parameter space of the Λ potentials by varying the Taylor coefficients of the Λ potential and the effective mass of Λ at the saturation density. Our analysis demonstrates that the parameter region consistent with the Λ binding energy data spans a wide range of the parameter space, including even more repulsive potentials than the χEFT prediction. We confirm that these strong repulsive Λ potentials suppress the presence of Λ in neutron star matter. We found that the Λ potentials repulsive at high densities are favored when the depth of the Λ potential at the saturation density, $U_\Lambda(\rho_0) = J_\Lambda$, is $J_\Lambda \gtrsim -29$ MeV, while attractive ones are favored when $J_\Lambda \lesssim -31$ MeV. This suggests that future high-resolution data of hypernuclei could rule out the scenario in which Λ's appear through the precise determination of J_Λ within the accuracy of 1 MeV.

DOI: 10.1103/PhysRevC.108.065803

I. INTRODUCTION

Neutron stars are gravitationally bound objects made of cold, extremely dense, and strongly interacting matter, which has a rich phase structure of quantum chromodynamics (QCD) [1]. They provide a unique cosmic laboratory for studying matter under extreme conditions. The inner structure of neutron stars is one of the important subjects in astrophysics and nuclear physics. Based on astrophysical observations and nuclear experiments, possibilities of various exotic states inside neutron stars have been theoretically discussed, including the admixture of hyperons [2–7] and the transition from hadron to quark matter [1,8–13].

In the 20th century, hyperons were predicted to admix in the neutron star matter at a density of 2–4 ρ_0, with the saturation density being $\rho_0 \simeq 0.16$ fm^{-3}, from phenomenological models [2–6] based on experimental data such as hypernuclear spectroscopy. The admixture of the hyperons softens the equation of state (EOS) of neutron star matter and reduces the maximum allowed mass of neutron stars significantly. For this reason, hyperonic matter EOSs constrained by hypernuclear data [2,4,14] or *G*-matrix calculations using two-body hyperon-nucleon (*YN*) interactions [5,6,15] could not sustain the observed massive neutron stars with $M \gtrsim 2M_\odot$ [16–20]. This problem is known as the hyperon puzzle in neutron stars and has been attracting the attention of nuclear physics and astrophysics researchers. A number of possible scenarios to solve the hyperon puzzle have been proposed, such as repulsive hyperon potentials at high densities caused by many-body baryon interactions [15,21–30], hyperon-hyperon (*YY*) repulsion [7,31,32], and a continuous transition to quark matter before the hyperon admixture [1,13], yet the definitive answer to the puzzle has not been found so far.

In the following, we shall explore the first scenario: the repulsive hyperon potential at high densities caused by many-baryon interactions. The three-nucleon repulsion is known to be necessary to explain the nuclear matter saturation point. Therefore, it is worthwhile to examine the impact of the *YNN* (*YYN*, *YYY*) three-baryon repulsion on the neutron star matter EOS. Several models including many-body interactions have been investigated by a multi-Pomeron exchange potential (MPP) based on the extended soft core (ESC) model [22,24–26] and the KIDS (Korea-IBS-Daegu-SKKU) density functional formalism [30]. These results show that repulsive three-baryon forces, which reproduce the binding energies of Λ hypernuclei, may solve the hyperon puzzle.

The chiral effective field theory (χEFT) provides a systematic and model-independent approximation of QCD at low densities [33]. The three-body forces were found to cause repulsive Λ potential at high densities in the χEFT [23,28,29,34] with the decuplet saturation model for the three-baryon interactions [35]. This Λ potential, $U_\Lambda^{\rm chi3}$, can prevent Λ from appearing in neutron stars [23] so that we can avoid the hyperon puzzle. The proposed Λ potential $U_\Lambda^{\rm chi3}$ should be validated by experiments and observations. In particular, the density dependence [23,34] and the momentum dependence [34] of the Λ potential $U_\Lambda^{\rm chi3}$ can be tested with different types

*Deceased.

of experimental data, such as the observables from heavy-ion collisions and the Λ binding energies of hypernuclei.

Heavy-ion collision experiments provide a unique opportunity to study the properties of QCD matter under various densities and temperatures. In the past two decades, a quark-gluon plasma of high temperature and low baryon density has been created and actively studied [36,37] using heavy-ion collisions at the top energies of the Relativistic Heavy Ion Collider (RHIC) and the Large Hadron Collidier (LHC). In recent heavy-ion experiments at lower energies, such as RHIC Beam Energy Scan [38] and NA61/SHINE programs [39], two colliding nuclei are compressed to form high baryon-density matter. In this regime, the anisotropic flows are known to be sensitive to the hadronic potentials at high densities [40]. The transport model calculation [41,42] using the event generator JAM2 [43] with the Λ potential $U_\Lambda^{\rm chi3}$ explains the collision energy dependence of the proton and Λ directed flow slopes (dv_1/dy) in Au+Au collisions within a relative precision of around 20% in the collision energy range of $3 \leqslant \sqrt{s_{NN}} \leqslant 19.6$ GeV [44–46]. However, it is found in Ref. [42] that the directed flow of Λ is not very sensitive to the density dependence of the Λ potential while it is sensitive to the momentum dependence. We should investigate further observables sensitive to the density dependence.

As another experimental observable to test $U_\Lambda^{\rm chi3}$, the up-to-date data of the Λ binding energies in hypernuclei provide useful constraints. The density dependence of the Λ potential at lower densities $\rho < \rho_0$ can be constrained by the Λ binding energies [47] while the momentum dependence is sensitive to the energy difference between orbitals of the Λ binding energy through the effective mass [48]. The Λ potentials LY-IV [49] and HPΛ2 [50] reproduce the Λ binding energy for hypernuclei in a wide range of mass number. Millner *et al.* [47] pointed out that the density dependence at higher densities determined by the best fitting to the Λ binding energy largely depends on the fitting form while the density dependence at lower densities is well constrained. However, the Λ potential $U_\Lambda^{\rm chi3}$ has a distinct shape from LY-IV and HPΛ2: it is more attractive at $\rho < \rho_0$ and has a larger value of the effective mass than LY-IV and HPΛ2. Thus, it should be tested whether $U_\Lambda^{\rm chi3}$ can reproduce the Λ binding energy data. In Ref. [51], the Λ potential based on the next-to-leading order (NLO) χEFT [52,53] that includes only two-body interaction has been tested by the *G*-matrix calculation. This two-body interaction only partially reproduces the observed binding energies for hypernuclei with mass number $A > 12$.

In this paper, we show that the Λ potential $U_\Lambda^{\rm chi3}$ from the χEFT [23,34], which is repulsive at high densities, can reproduce the experimental data of the Λ binding energies with the Skyrme-Hartree-Fock method [49,50,54–56]. These results mean that the two distinct Λ potentials—repulsive and attractive Λ potentials at high densities—can reproduce the same experimental Λ binding energy. Here, we carry out a global parameter search for the Λ potentials to scan a wider range of the Λ potentials and evaluate the uncertainty range. We parametrize the Λ potential by the effective mass and the Taylor coefficients at ρ_0. We examine different Λ potentials by varying the parameters and identify the parameter space consistent with the experimental data. Finally, we discuss the parameter region of the Λ potentials which suppresses Λ's in neutron star matter.

This paper is organized as follows. In Sec. II, we introduce the Skyrme-Hartree-Fock method for the Λ hypernuclei with the Λ potential from the χEFT and compare the Λ binding energies with existing models and the experimental data. In Sec. III, we search for the favored region of the effective mass and the Taylor coefficients of the Λ potential. In Sec. IV, we discuss the admixture of Λ in neutron star matter for various Λ potentials which reproduce the binding energy of Λ hypernuclei. The conclusion and outlook are given in Sec. V.

II. Λ BINDING ENERGY FROM THE χEFT

To explain the Λ binding energies of Λ hypernuclei from middle to large mass numbers, mean-field calculations of self-consistent calculations have been successfully employed, including Skyrme-Hartree-Fock methods [30,49,50,54–57], relativistic mean-field models [7,58–60], and *G*-matrix calculations [22,29].

We employ the Skyrme-Hartree-Fock method to compute the binding energy of Λ hypernuclei using the Skyrme-type Λ potential parametrizing the results of the χEFT.

A. Skyrme-Hartree-Fock method for Λ hypernuclei

In this study, the wave function of the Λ hypernuclei ${}^{A}_{\Lambda}Z$ with mass number A and proton number Z is taken as [54]

$$\Phi_{\rm hyp} = \phi_\Lambda \Phi_{\rm core}, \tag{1}$$

where $\phi_\Lambda(\boldsymbol{r}, \sigma)$ is the single-particle wave function of Λ, with $\boldsymbol{r}$ and $\sigma = \pm 1/2$ being the spatial and spin coordinates, respectively. The Slater determinant $\Phi_{\rm core}$ is constructed from $A-1$ nucleon single-particle wave functions $\phi_i(\boldsymbol{r}, q, \sigma)$ with $q = \pm 1/2$ being the isospin. The Skyrme-type baryon-baryon interaction with one Λ hyperon is expressed as

$$\begin{aligned} V &= V^{NN} + V^{\Lambda N} \\ &= \sum_{i<j}^{A-1} v^{NN}(\boldsymbol{r}_i, \boldsymbol{r}_j) + \sum_{i=1}^{A-1} v^{\Lambda N}(\boldsymbol{r}_\Lambda, \boldsymbol{r}_i), \end{aligned} \tag{2}$$

where $\boldsymbol{r}_i$ and $\boldsymbol{r}_\Lambda$ are the spatial coordinates of the ith nucleon and Λ, respectively. We use the SLy4 parametrization [61] for the nucleon-nucleon interaction v^{NN}. The following Λ-nucleon interaction $v^{\Lambda N}$ is assumed as in Refs. [30,49,55]:

$$\begin{aligned} &v^{\Lambda N}(\boldsymbol{r}_\Lambda, \boldsymbol{r}_N) \\ &= t_0^\Lambda \left(1 + x_0^\Lambda P_\sigma\right) \delta(\boldsymbol{r}_\Lambda - \boldsymbol{r}_N) \\ &\quad + \frac{1}{2} t_1^\Lambda [\overleftarrow{\boldsymbol{k}}^2 \delta(\boldsymbol{r}_\Lambda - \boldsymbol{r}_N) + \delta(\boldsymbol{r}_\Lambda - \boldsymbol{r}_N) \overrightarrow{\boldsymbol{k}}^2] \\ &\quad + t_2^\Lambda \overleftarrow{\boldsymbol{k}}\, \delta(\boldsymbol{r}_\Lambda - \boldsymbol{r}_N) \cdot \overrightarrow{\boldsymbol{k}} \\ &\quad + \frac{3}{8} t_{3,1}^\Lambda (1 + x_{3,1}^\Lambda P_\sigma) \delta(\boldsymbol{r}_\Lambda - \boldsymbol{r}_N) \rho_N^{\gamma_1} \left(\frac{\boldsymbol{r}_N + \boldsymbol{r}_\Lambda}{2} \right) \\ &\quad + \frac{3}{8} t_{3,2}^\Lambda (1 + x_{3,2}^\Lambda P_\sigma) \delta(\boldsymbol{r}_\Lambda - \boldsymbol{r}_N) \rho_N^{\gamma_2} \left(\frac{\boldsymbol{r}_N + \boldsymbol{r}_\Lambda}{2} \right), \end{aligned} \tag{3}$$

where t_k^Λ, $t_{k,l}^\Lambda$, x_k^Λ, and $x_{k,l}^\Lambda$ are the Skyrme potential parameters. The spin-exchange operator is given by $P_\sigma = (1 + \boldsymbol{\sigma}_\Lambda \cdot \boldsymbol{\sigma}_N)/2$ with $\boldsymbol{\sigma}_\Lambda$ and $\boldsymbol{\sigma}_N$ being the Pauli matrices acting on the spin wave functions of Λ and the nucleon, respectively. The derivatives $\overleftarrow{\boldsymbol{k}} = -(\overleftarrow{\nabla}_\Lambda - \overleftarrow{\nabla}_N)/2i$ and $\overrightarrow{\boldsymbol{k}} = (\overrightarrow{\nabla}_\Lambda - \overrightarrow{\nabla}_N)/2i$ operate on the left- and right-hand sides, respectively, where $\nabla_\Lambda = \partial/\partial \boldsymbol{r}_\Lambda$ and $\nabla_N = \partial/\partial \boldsymbol{r}_N$. The symbol $\rho_N(\boldsymbol{r}_N)$ denotes the nucleon density specified later. The $\rho_N^{\gamma_1}$ term with $\gamma_1 = 1/3$, which is motivated by the expansion in the Fermi momentum ($\propto \rho_N^{1/3}$), is needed for the Skyrme-type Λ potential to reproduce the G-matrix result of the Λ potential [49]. The $\rho_N^{\gamma_2}$ term with $\gamma_2 = 2/3$ is added to reproduce the results from the χEFT [23]. The spin-orbit force is neglected in this work because it is expected to be small from the experimental data [62,63]. The pairing correlation is not considered either.

The expectation value of the total energy for the Λ hypernuclei $\mathcal{E}_{\rm hyp}$ is obtained as

$$\begin{aligned}\mathcal{E}_{\rm hyp} &= \langle \Phi_{\rm hyp}|T + V|\Phi_{\rm hyp}\rangle - \mathcal{E}_{\rm c.m.} \\ &= \mathcal{E}_N + \mathcal{E}_\Lambda - \mathcal{E}_{\rm c.m.},\end{aligned} \tag{4}$$

where

$$T = T_N + T_\Lambda = -\sum_{i=1}^{A-1} \frac{\hbar^2 \nabla_i^2}{2m_i} - \frac{\hbar^2 \nabla_\Lambda^2}{2m_\Lambda} \tag{5}$$

is the kinetic energy operator, and m_i and m_Λ are the masses of the nucleon and Λ, respectively. The energies $\mathcal{E}_N$ and $\mathcal{E}_\Lambda$ are contributions from $T_N + V^{NN}$ and $T_\Lambda + V^{\Lambda N}$, respectively. The total energy of Λ takes the following form:

$$\mathcal{E}_\Lambda = \int \mathrm{d}^3 r H_\Lambda, \tag{6}$$

$$\begin{aligned}H_\Lambda = &\frac{\hbar^2}{2m_\Lambda}\tau_\Lambda + a_1^\Lambda \rho_N \rho_\Lambda \\ &+ a_2^\Lambda(\tau_\Lambda \rho_N + \tau_N \rho_\Lambda) - a_3^\Lambda(\rho_\Lambda \cdot \Delta\rho_N) \\ &+ a_4^\Lambda \rho_N^{1+\gamma_1}\rho_\Lambda + a_5^\Lambda \rho_N^{1+\gamma_2}\rho_\Lambda,\end{aligned} \tag{7}$$

where H_Λ is the energy density of Λ, and the coefficients a_i^Λ are related to the parameters in the Λ-nucleon interaction $v^{\Lambda N}$ as

$$\begin{aligned}a_1^\Lambda &= t_0^\Lambda\left(1 + \frac{1}{2}x_0^\Lambda\right), \quad a_2^\Lambda = \frac{1}{4}\left(t_1^\Lambda + t_2^\Lambda\right), \\ a_3^\Lambda &= \frac{1}{8}\left(3t_1^\Lambda - t_2^\Lambda\right), \quad a_4^\Lambda = \frac{3}{8}t_{3,1}^\Lambda\left(1 + \frac{1}{2}x_{3,1}^\Lambda\right), \\ a_5^\Lambda &= \frac{3}{8}t_{3,2}^\Lambda\left(1 + \frac{1}{2}x_{3,2}^\Lambda\right).\end{aligned}$$

The densities ρ_N, τ_N, ρ_Λ, and τ_Λ are defined as

$$\rho_N = \sum_{i=1}^{A-1}|\phi_i|^2, \quad \tau_N = \sum_{i=1}^{A-1}|\nabla\phi_i|^2, \tag{8}$$

$$\rho_\Lambda = |\phi_\Lambda|^2, \quad \tau_\Lambda = |\nabla\phi_\Lambda|^2. \tag{9}$$

The center-of-mass energy $\mathcal{E}_{\rm c.m.}$ in Eq. (4) is approximated by the average of the center-of-mass kinetic operator neglecting the cross terms [54],

$$\mathcal{E}_{\rm c.m.} \simeq \int \mathrm{d}^3 r \frac{\hbar^2(\tau_N + \tau_\Lambda)}{2[Zm_p + (A - Z - 1)m_n + m_\Lambda]}. \tag{10}$$

The Hartree-Fock equations for single-particle wave functions ϕ_i ($i = 1, 2, \ldots, A-1, \Lambda$) are derived from the variational equation:

$$\frac{\delta}{\delta\phi_i}\left(\mathcal{E}_{\rm hyp} - \sum_{i=1}^{A-1}\epsilon_i\int \mathrm{d}^3 r|\phi_i|^2 - \epsilon_\Lambda\int \mathrm{d}^3 r|\phi_\Lambda|^2\right) = 0, \tag{11}$$

where ϵ_i is the single-particle energy. Equation (11) combined with Eq. (4) yields the equation for the single-particle wave function of the ith particle with the baryon type $B_i = p, n, \Lambda$,

$$\left[-\nabla\cdot\left(\frac{\hbar^2}{2m_{B_i}^*(\boldsymbol{r})}\nabla\right) + V_{B_i}(\boldsymbol{r}) - i\boldsymbol{W}_{B_i}(\boldsymbol{r})\cdot(\nabla\times\boldsymbol{\sigma})\right]\phi_i = \epsilon_i\phi_i. \tag{12}$$

The first term is the kinetic energy including the effective mass, the second is the single-particle potential, and the third is the spin-orbit potential. The expressions for those terms are specified below.

In this work, we assume spherical symmetry of the hypernuclei as in Refs. [30,49,50,54–56]. We assign the principle quantum number n, the orbital angular momentum ℓ, the total angular momentum j, and the magnetic quantum number m_j to each i. The single-particle wave function for the ith nucleon with the isospin q is expressed as

$$\phi_i(\boldsymbol{r}, q) = \frac{R_\alpha(r)}{r}\mathcal{Y}_{l\,jm_j}(\hat{\boldsymbol{r}})\chi_q, \quad \alpha = \{nl\,jq\}, \tag{13}$$

where $r = |\boldsymbol{r}|$, $\hat{\boldsymbol{r}} = \boldsymbol{r}/|\boldsymbol{r}|$, and

$$\mathcal{Y}_{l\,jm_j}(\hat{\boldsymbol{r}}) = \sum_{m_l m_s}\langle lm_l\,1/2\,m_s|jm_j\rangle Y_{lm_l}(\hat{\boldsymbol{r}})\chi_{m_s}. \tag{14}$$

The symbols χ_q and χ_{m_s} denote the isospin and spin wave functions, respectively, and Y_{lm_l} is the spherical harmonics. The Λ single-particle wave function is similarly written as

$$\phi_\Lambda(\boldsymbol{r}) = \frac{R_\alpha(r)}{r}\mathcal{Y}_{l\,jm_j}(\hat{\boldsymbol{r}}). \tag{15}$$

The Skyrme-Hartree-Fock equation (12) is reduced to the equation for the radial wave function R_α:

$$\begin{aligned}&-\frac{\hbar^2}{2m_{B_\alpha}^*}R_\alpha''(r) - \frac{\mathrm{d}}{\mathrm{d}r}\left(\frac{\hbar^2}{2m_{B_\alpha}^*}\right)R_\alpha'(r) \\ &\quad + \left[\frac{\hbar^2}{2m_{B_\alpha}^*}\frac{l_\alpha(l_\alpha+1)}{r^2} + V_{B_\alpha}(r) + \frac{1}{r}\frac{\mathrm{d}}{\mathrm{d}r}\left(\frac{\hbar^2}{2m_{B_\alpha}^*}\right)\right. \\ &\quad \left. + \frac{W_{B_\alpha}}{r}\left(j_\alpha(j_\alpha+1) - l_\alpha(l_\alpha+1) - \frac{3}{4}\right)\right]R_\alpha(r) \\ &= \epsilon_\alpha R_\alpha(r).\end{aligned} \tag{16}$$

For nucleons, the explicit forms of $m^*_{B_\alpha}$, V_{B_α}, and W_{B_α} are found in Appendix A. For Λ, they are expressed as

$$\frac{\hbar^2}{2m^*_\Lambda} = \frac{\hbar^2}{2m_\Lambda} + a_2^\Lambda \rho_N, \tag{17}$$

$$V_\Lambda = a_1^\Lambda \rho_N + a_2^\Lambda \tau_N - a_3^\Lambda \Delta\rho_N + a_4^\Lambda {\rho_N}^{1+\gamma_1} + a_5^\Lambda {\rho_N}^{1+\gamma_2}. \tag{18}$$

In the case of the open-shell nuclei, we employ the filling approximation [64]: when there are m nucleons in the open shell, they are filled in the highest j states at the same occupation probability $m/(2j+1)$. Similarly, Λ occupies each state of j with an occupation probability $1/(2j+1)$. Then, the Λ density is calculated as

$$\rho_\Lambda(r) = \frac{1}{2j+1}\sum_{m_j}\left|\frac{R_\alpha(r)}{r}\mathcal{Y}_{ljm_j}\right|^2 = \frac{R_\alpha^2(r)}{4\pi r^2}. \tag{19}$$

After solving Eq. (12) self-consistently, the Λ binding energy is obtained as

$$B_\Lambda = -(\mathcal{E}_{\rm hyp} - \mathcal{E}_{\rm core}), \tag{20}$$

where the total energy of the core nucleus $\mathcal{E}_{\rm core}$ is independently calculated by solving the self-consistent equation for the Slater determinant of the core nucleus.

B. Skyrme-type Λ potentials from the χEFT

In this subsection, we parametrize the Λ potentials obtained from the χEFT assuming the form of the density and momentum dependence in Eq. (7). In uniform matter, the kinetic density τ_Λ becomes

$$\tau_\Lambda = |\nabla\phi_\Lambda|^2 = k_\Lambda^2|\phi_\Lambda|^2 = k_\Lambda^2\rho_\Lambda, \tag{21}$$

with k_Λ being the momentum of Λ. Then, the Λ single-particle potential in uniform nuclear matter at zero temperature is obtained as

$$U_\Lambda(\rho_N, k_\Lambda) = \frac{\delta}{\delta\rho_\Lambda}\left[H_\Lambda - \frac{\hbar^2}{2m_\Lambda}\tau_\Lambda\right] = a_1^\Lambda\rho_N + a_2^\Lambda\left(k_\Lambda^2\rho_N + \tau_N\right) + a_4^\Lambda\rho_N^{1+\gamma_1} + a_5^\Lambda\rho_N^{1+\gamma_2}, \tag{22}$$

with

$$\tau_N = \tau_p + \tau_n, \tag{23}$$

$$\tau_q = \frac{3}{5}(3\pi^2)^{2/3}\rho_q^{5/3}, \quad q = p, n, \tag{24}$$

$$\gamma_1 = 1/3, \quad \gamma_2 = 2/3. \tag{25}$$

The Skyrme potential parameters of Λ, a_i^Λ, are determined by the fitting to the potentials from the χEFT of Ref. [23] (GKW) and Ref. [34] (Kohno).

We first fix the momentum-dependent part of the Λ potential a_2^Λ at the saturation density $\rho_0 = 0.16$ fm^{-3} by using the results of Ref. [34]. Figure 1 shows the momentum dependence of the Λ single-particle potential. Kohno3 in Fig. 1 is obtained by including the ΛNN three-body interaction using the decuplet saturation model [35]. Kohno2 in Fig. 1 is obtained using only the two-body force. Because the depth of the Λ potential at the saturation density differs between GKW [23] and Kohno [34], we subtract the value at $k_\Lambda = 0$ fm^{-1} from the Λ potential as $U_\Lambda(k_\Lambda) - U_\Lambda(k_\Lambda = 0\ \text{fm}^{-1})$ and use it in fitting the momentum dependence of the Λ potential. Chi2 and Chi3 in Fig. 1 are the fitting results of Kohno2 and Kohno3 at $k_\Lambda < 1.5$ fm, respectively.

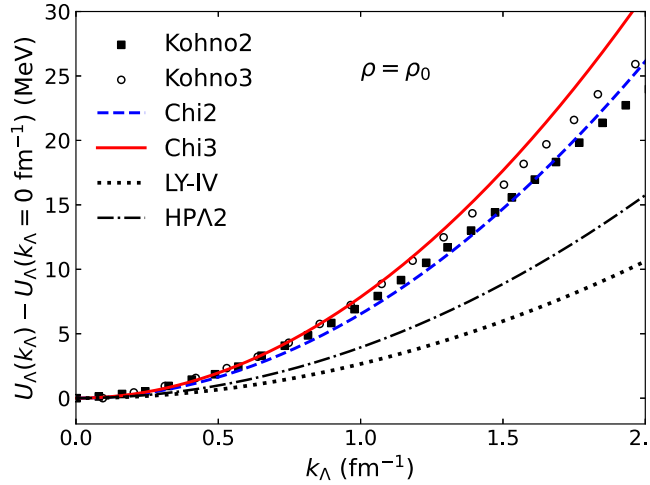

FIG. 1. Momentum dependence of the Λ potentials in symmetric nuclear matter at the saturation density with its value at zero momentum subtracted. Kohno2 and Kohno3 represent the results of the Λ single-particle potential with only two-body interactions and two- and three-body interactions [34] from the χEFT [34], respectively. Solid and dashed lines represent the fitting results to Kohno2 and Kohno3, respectively. The dotted and dash-dotted lines correspond to the Λ potentials LY-IV [49] and HPΛ2 [50], respectively.

For the remaining Skyrme potential parameters, we consider the density dependence of the Λ potential obtained from the χEFT [23]. In Fig. 2, GKW2 (GKW3) is the result from the χEFT with ΛN ($\Lambda N + \Lambda NN$) interaction. The ΛNN three-body interaction in GKW3 is calculated by the decuplet saturation model [35]. The parameters $(a_1^\Lambda, a_4^\Lambda, a_5^\Lambda)$ of Chi2 (Chi3) are obtained by fitting Eq. (22) to the upper and lower lines of GKW2 (GKW3) and taking the average.

Unlike the previous work [42], where we fitted the data in the region $\rho/\rho_0 < 3.5$, the fitting region in the present study is limited to $\rho/\rho_0 < 1.5$ in order to reproduce the GKW results in the low-density region more accurately. The resultant Skyrme parameters a_1^Λ, a_2^Λ, a_4^Λ, and a_5^Λ from the fitting are listed in Table I. The fitting results accurately reproduce the χEFT results at $\rho/\rho_0 \lesssim 1.0$, which is relevant for calculating the Λ hypernuclei.

For comparison, the Λ potentials that are used to explain the Λ binding energy data (LY-IV [49] and HPΛ2 [50]) are shown in Figs. 1 and 2. The LY-IV and HPΛ2 Λ potentials exhibit different characteristics compared to the potentials obtained from the χEFT. Specifically, they display enhanced repulsion in low-density regions, increased attraction in high-density regions, and a weaker momentum dependence.

Because the Skyrme parameter a_3^Λ cannot be determined by fitting the results in the uniform matter, we determine a_3^Λ

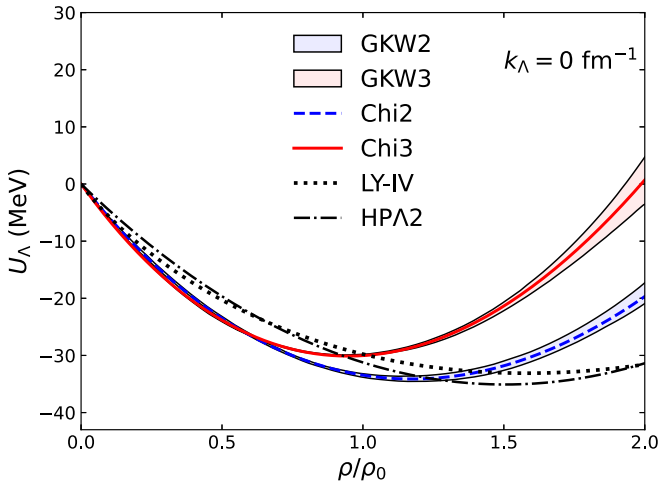

FIG. 2. Normalized baryon density dependence of the single-particle potentials for Λ in symmetric nuclear matter. GKW2 and GKW3 represent the results of the Λ single-particle potential with only two-body interactions and with two- and three-body interactions obtained from the χEFT [23], respectively. The solid and dashed lines represent the fitting results to GKW2 and GKW3, respectively. The dotted and dash-dotted lines correspond to the Λ potentials LY-IV [49] and HPΛ2 [50], respectively.

to reproduce the experimental value of the Λ binding energy of ${}^{13}_{\Lambda}$C, 11.88 MeV. The experimental value is taken from Ref. [65] with a correction of 0.5 MeV, which is pointed out in Ref. [66]. There are two reasons for choosing ${}^{13}_{\Lambda}$C: First, it has a larger surface-energy effect compared with a heavier nucleus. Second, the spherical Skyrme-Hartree-Fock method is expected to provide a relatively good description of ${}^{13}_{\Lambda}$C because it has even numbers of protons and neutrons.

We show in Table I the Taylor coefficients and the normalized effective mass at ρ_0, which characterize the Λ potential:

$$J_\Lambda = U_\Lambda(\rho_N = \rho_0, k_\Lambda = 0), \tag{26}$$

$$L_\Lambda = 3\rho_N \frac{\partial U_\Lambda}{\partial \rho_N}\bigg|_{\rho_N=\rho_0,k_\Lambda=0}, \tag{27}$$

$$K_\Lambda = 9\rho_N^2 \frac{\partial^2 U_\Lambda}{\partial \rho_N^2}\bigg|_{\rho_N=\rho_0,k_\Lambda=0}, \tag{28}$$

$$\frac{m_\Lambda^*}{m_\Lambda}\bigg|_{\rho_N=\rho_0} = \frac{1}{1+\frac{2m_\Lambda}{\hbar^2}a_2^\Lambda \rho_0}. \tag{29}$$

C. Λ single-particle potential and Λ binding energy

We now present the results of the Skyrme-Hartree-Fock calculations for Λ hypernuclei using the Λ Skyrme interaction discussed in the previous section.

Figure 3 shows the Λ single-particle potential (18) for hypernucleus ${}^{208}_{\Lambda}$Pb. At a distance $r < 4$ fm where the nucleon density ρ_N is close to the saturation density ρ_0, both Chi3 and LY-IV have the potential depth of −30 MeV while Chi2 has a slightly greater depth of −33 MeV. Those values reflect J_Λ, the Λ-potential depth at ρ_0 (see Table I).

TABLE I. The sets of Skyrme potential parameters are listed above the gap between γ_2 and J_Λ. Chi2 and Chi3 are the fitting results to the χEFT calculations [23,34]. LY-IV [49] and HPΛ2 [50] are the Λ potentials which can explain the Λ binding energy data. We also list the values that characterize potentials: the Taylor coefficients (J_Λ, L_Λ, K_Λ) and the normalized effective mass m_Λ^*/m_Λ at ρ_0 defined by Eqs. (26)–(29). The mean squared deviation of the calculated Λ binding energy from the experimental data ΔB_Λ is defined by Eq. (30).

	Chi2	Chi3	LY-IV	HPΛ2
t_0^Λ (MeV fm^3)	−352.2	−388.3	−542.5	−399.9
t_1^Λ (MeV fm^5)	143.7	120.4	56.0	83.4
t_2^Λ (MeV fm^5)	13.7	68.7	8.0	11.5
$t_{3,1}^\Lambda$ (MeV fm^4)	−951.9	−1081.8	1387.9	2046.8
$t_{3,2}^\Lambda$ (MeV fm^5)	2669	3351	0	0
x_0^Λ	0	0	−0.153	−0.486
$x_{3,1}^\Lambda$	0	0	0.107	−0.660
$x_{3,2}^\Lambda$	0	0	0	0
γ_1	1/3	1/3	1/3	1
γ_2	2/3	2/3	0	0
J_Λ (MeV)	−33.5	−30.0	−29.8	−31.2
L_Λ (MeV)	−23.5	9.3	−36.2	−46.1
K_Λ (MeV)	415	532	218	277
m_Λ^*/m_Λ	0.73	0.70	0.87	0.82
ΔB_Λ (MeV)	1.55	0.72	0.71	0.78

Figure 4 compares the Λ binding energies calculated from different Λ potentials at mass number $A = 13$–208 in $1s$, $1p$, $1d$, $1f$, and $1g$ orbitals. The experimental data at $A = 16$–208 are listed in Table III. Chi3, which includes the ΛNN three-body force, reproduces the data. This implies that the strong repulsive Λ potential, which is sufficient to suppress the pres-

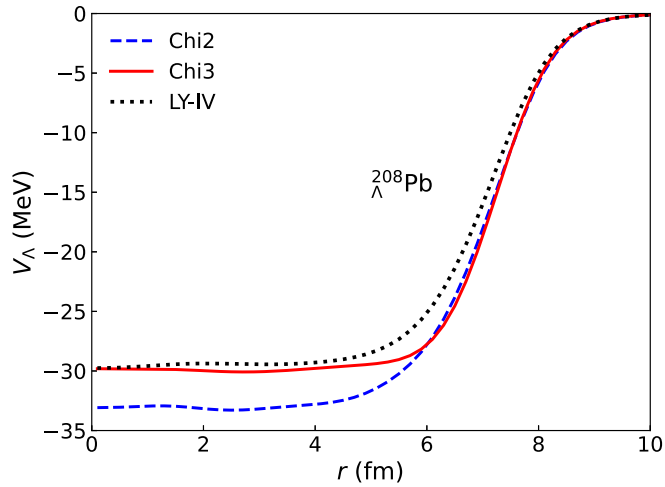

FIG. 3. Λ single-particle potential (18) for hypernucleus ${}^{208}_{\Lambda}$Pb in the coordinate space. The dashed and solid lines show the results from the Λ potentials Chi2 and Chi3, respectively. The dotted line corresponds to the result from the LY-IV parameter sets.

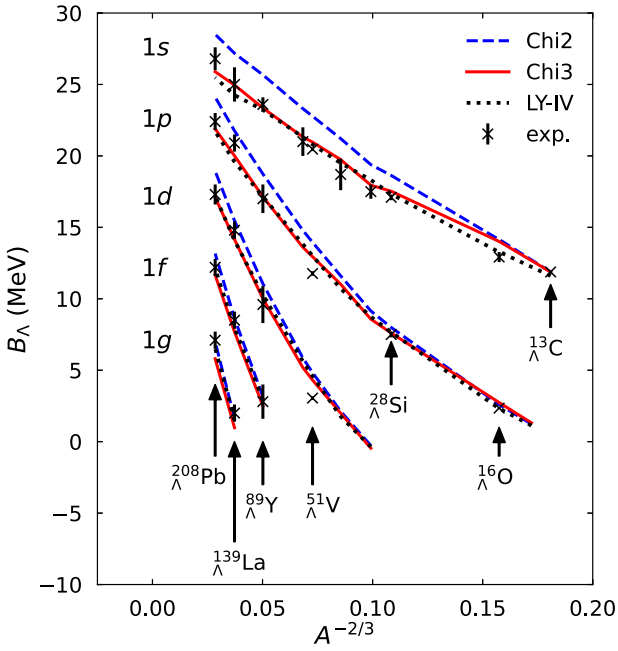

FIG. 4. Calculated Λ binding energies of $1s$, $1p$, $1d$, $1f$, and $1g$ orbitals as a function of $A^{-2/3}$, where A is the mass number of hypernuclei. Chi2 and Chi3 represent the results using the Λ single-particle potential with only two-body and with two- and three-body interactions from the χEFT, respectively. The dotted line corresponds to the result using the LY-IV Λ potential. The crosses indicate the experimental data.

ence of Λ hyperons in dense nuclear matter, is consistent with the observed Λ hypernuclear data. On the other hand, Chi2, which includes only the ΛN two-body force, predicts the overbinding of the data in the $1s$ orbital. This is because J_Λ is as deep as approximately −33 MeV for Chi2. We note that Chi2 and Chi3 have almost the same effective mass. These results indicate the necessity of three-baryon interaction to reproduce the binding energy of Λ, which is consistent with the findings in Refs. [22,67,68].

The last row of Table I shows the root-mean-square deviation of the model calculation from the experimental data,

$$\Delta B_\Lambda = \sqrt{\frac{1}{N_{\rm data}} \sum_i^{N_{\rm data}} \left(B^{\rm exp}_{\Lambda,i} - B^{\rm cal}_{\Lambda,i}\right)^2}, \tag{30}$$

where $N_{\rm data}$ is the number of the experimental data, and $B^{\rm exp}_{\Lambda,i}$ ($B^{\rm cal}_{\Lambda,i}$) is the experimental (calculated) Λ binding energy of nuclide i. The experimental data $B^{\rm exp}_{\Lambda,i}$ are listed in Table III. We avoid using the chi squared because it is hard to quantify the systematic error of our mean-field calculation. Neglecting the model error in the chi-square would cause an excessive fitting to lighter hypernuclei, for which the experimental data has a smaller error while the mean-field calculation would have a larger error. Chi3 is found to be consistent with the experimental data at the same level of accuracy as the Λ potentials LY-IV, with the value of $\Delta B_\Lambda \approx 0.7$ MeV. The HPΛ2 potential has a larger $\Delta B_\Lambda = 0.78$ MeV because it is parametrized by chi-square minimization using the data without the correction of 0.5 MeV [66].

III. PARAMETER SEARCH FOR Λ POTENTIALS

In the previous section, we showed that both the repulsive and attractive Λ potentials at high densities, Chi3 and LY-IV, reproduce the Λ binding energy data. This is because the Λ binding energy is mostly determined by the potential values at low densities. However, another attractive potential, HPΛ2, does not reproduce the data at the same level as Chi3 and LY-IV, which suggests that the details of the potential, including the values of the Taylor coefficients, are important for the Λ binding energy. In this section, we will investigate the parameter space of the Λ potential that can reproduce the binding energy of the Λ hypernuclear data. From this analysis, we expect constraints on the relations among the Taylor coefficients (26)–(28) and the normalized effective mass (29). These constraints can restrict the repulsion of the Λ potential at high densities similarly to the nuclear matter EOS.

A. Procedure

The symmetry-energy parameters of nuclear matter are used to examine the nuclear matter EOS at high densities using the behavior around ρ_0 [69]. Similarly, to investigate the parameter space of the Λ potential, we parametrize the Skyrme-type Λ potential (22) by the Taylor coefficients (26)–(28) and the normalized effective mass m^*_Λ/m_Λ at the saturation density. We generate $13 \times 25 \times 21 \times 21 = 143325$ parameter sets of $(J_\Lambda, L_\Lambda, K_\Lambda, m^*_\Lambda/m_\Lambda)$ as combinations of the following parameter points:

$$J_\Lambda = -33, -31.5, -32, \ldots, -27 \text{ MeV}, \tag{31a}$$

$$L_\Lambda = -50, -45, -40, \ldots, 70 \text{ MeV}, \tag{31b}$$

$$K_\Lambda = 0, 50, 100, \ldots, 1000 \text{ MeV}, \tag{31c}$$

$$\frac{m^*_\Lambda}{m_\Lambda} = 0.5, 0.525, 0.55, \ldots, 1.00. \tag{31d}$$

The range of J_Λ is chosen to be consistent with the Λ binding energy data of the $1s$ orbital: J_Λ below the range overestimates the data, and vice versa. The effective mass m^*_Λ/m_Λ has upper and lower limits because it is sensitive to the separation of the Λ binding energies between different orbitals. The second derivative K_Λ has a lower limit of 0 MeV because the Λ potential should become repulsive at high densities. We note that these parameters in the existing models shown in Table I fall within the above parameter ranges.

For each parameter set of $(J_\Lambda, L_\Lambda, K_\Lambda, m^*_\Lambda/m_\Lambda)$, the Skyrme potential parameters a^Λ_i are determined in the following procedure. First, a^Λ_2 is determined from its relation to the effective mass (29):

$$a^\Lambda_2 = \frac{1}{\rho_0}\frac{\hbar^2}{2m_\Lambda}\left(\frac{1}{m^*_\Lambda/m_\Lambda} - 1\right). \tag{32}$$

The potential parameters a^Λ_1, a^Λ_4, and a^Λ_5 are determined by solving the following relations obtained from Eqs. (26)–(28) with $\gamma_1 = 1/3$ and $\gamma_2 = 2/3$:

$$J_\Lambda = a^\Lambda_1\rho_0 + a^\Lambda_2\tau_0 + a^\Lambda_4\rho_0^{4/3} + a^\Lambda_5\rho_0^{5/3}, \tag{33a}$$

$$L_\Lambda = 3a^\Lambda_1\rho_0 + 5a^\Lambda_2\tau_0 + 4a^\Lambda_4\rho_0^{4/3} + 5a^\Lambda_5\rho_0^{5/3}, \tag{33b}$$

$$K_\Lambda = 10a^\Lambda_2\tau_0 + 4a^\Lambda_4\rho_0^{4/3} + 10a^\Lambda_5\rho_0^{5/3}, \tag{33c}$$

where $\tau_0 = 3/5(3\pi^2/2)^{2/3}\rho_0^{5/3}$. The remaining parameter a_3^Λ is determined to reproduce the experimental value of the Λ binding energy of $^{13}_{\Lambda}$C, 11.88 MeV, which is taken from Ref. [65] with a correction of 0.5 MeV [66].

Using the determined potential parameters a_i^Λ for each parameter set, we calculate the Λ binding energy using the Skyrme-Hartree-Fock method as explained in Sec. II A. We evaluate the root-mean-square deviation ΔB_Λ (30) and select the parameter sets that satisfy $\Delta B_\Lambda < 0.75$ MeV. We hereafter call the Λ potentials with the selected parameter sets *selected* Λ *potentials* and the others *rejected* Λ *potentials*.

B. Results

We show the density dependence of the Λ potentials in the upper panel of Fig. 5, and the momentum dependence of the Λ potentials subtracting their values at $k_\Lambda = 0$ fm^{-1} in the lower panel of Fig. 5. The bold red lines indicate the selected Λ potentials. We found that the density dependence at high densities $\rho > \rho_0$ spreads more widely compared to the low-density region $\rho < \rho_0$. Namely, the Λ binding energy data constrain the Λ potential in the low-density region better than in the high-density region. We note that the spread of our results at $\rho < \rho_0$ is larger than that observed in Ref. [47]. This is because we considered the finite size of the uncertainty range of the Λ potential parameters, while Ref. [47] only shows the best fitting results by several functional forms.

In contrast to the density dependence of the Λ potentials, the magnitude of the momentum dependence has upper and lower limits, as shown in the lower panel of Fig. 5. The LY-IV and HPΛ2 potentials lie around the lower limit while the Chi3 potentials are close to the upper limit. The sensitivity of the energy separation between orbitals to the effective mass [48] constrains the momentum dependence of the Λ potential.

Let us now examine the correlations among the parameters of the selected Λ potentials. For this purpose, we choose two parameters from $(J_\Lambda, L_\Lambda, K_\Lambda, m_\Lambda^*/m_\Lambda)$ and plot ΔB_Λ as a function of the chosen parameters. We consider several choices of the two parameters as shown in Fig. 6. In calculating ΔB_Λ, the other parameters are optimized to minimize ΔB_Λ by using the golden-section search [70] within the ranges in Eqs. (31). For example, for the J_Λ-m_Λ^*/m_Λ plot in the top left panel of Fig. 6, the remaining parameters, L_Λ and K_Λ, are optimized for each point of $(J_\Lambda, m_\Lambda^*/m_\Lambda)$. The values of the optimized parameters are shown in Appendix C. The top left panel of Fig. 6 shows ΔB_Λ as functions of J_Λ and m_Λ^*/m_Λ. The selected parameter sets are within the ranges of $-31.5 < J_\Lambda < -28$ MeV and $0.65 < m_\Lambda^*/m_\Lambda < 0.95$. The potential depth J_Λ is consistent with the well-known results by the Woods-Saxon potential [47,71]. A positive correlation between J_Λ and m_Λ^*/m_Λ is found because the contribution of the kinetic-energy term $-\hbar^2\nabla_\Lambda^2/2m_\Lambda^*$ increases as the normalized effective mass m_Λ^*/m_Λ decreases. The HPΛ2 potential is located outside of the region of the selected Λ potentials because HPΛ2 was originally constructed through the chi-square minimization using the data without the 0.5 MeV

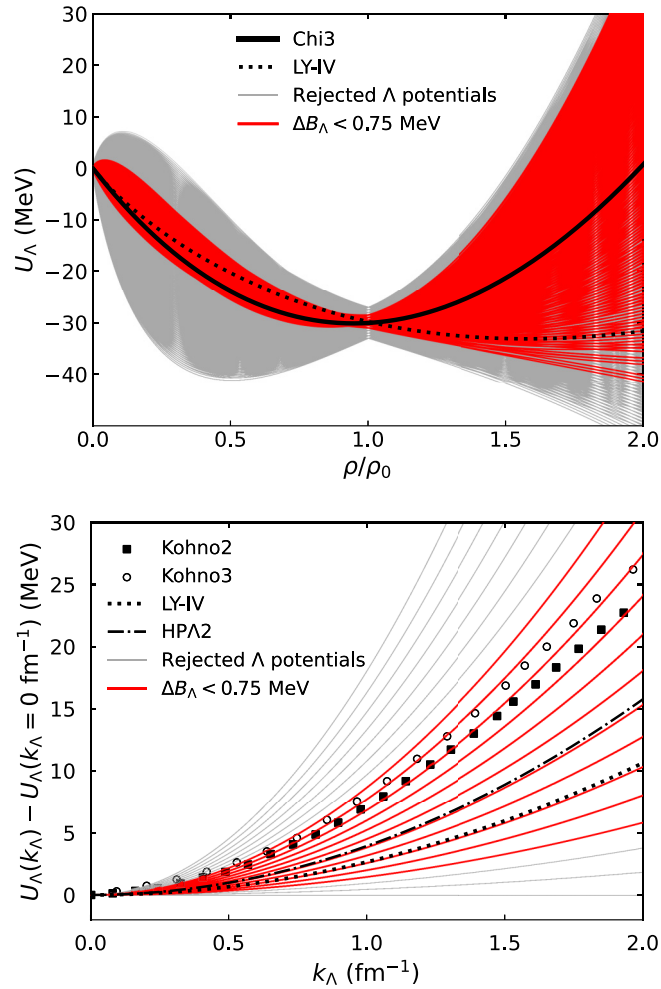

FIG. 5. The upper panel shows the density dependence in symmetric nuclear matter while the lower panel shows the momentum dependence of the Λ single-particle potentials. The thin gray lines represent all generated Λ potentials while the bold red lines are the selected Λ potentials with $\Delta B_\Lambda < 0.75$ MeV. Chi2 and Chi3 represent the result using the Λ single-particle potential with only two-body interactions and two- and three-body interactions from the χEFT, respectively. The dotted line corresponds to the result using the LY-IV Λ potential.

correction [66]. In the top right panel of Fig. 6, we show ΔB_Λ as functions of J_Λ and L_Λ. The region of the selected potentials is bounded from below, $L_\Lambda \gtrsim -45$ MeV, because the experimental data of the Λ binding energy cannot be reproduced with the Λ potential that is too shallow at $\rho < \rho_0$. In the bottom left panel of Fig. 6, we show ΔB_Λ as functions of J_Λ and K_Λ. The condition $\Delta B_\Lambda < 0.75$ MeV is satisfied for $K_\Lambda \gtrsim 50$ MeV. There is no upper limit in K_Λ, which implies that the Λ potential can be even more repulsive than the ones covered in this parameter search. In the bottom right panel of Fig. 6, we show ΔB_Λ as functions of L_Λ and K_Λ. For the region with $\Delta B_\Lambda < 0.75$ MeV, there is a positive correlation between L_Λ and K_Λ so that the effects of the two parameters compensate for each other at low densities at which the Λ potential is constrained. Larger values of

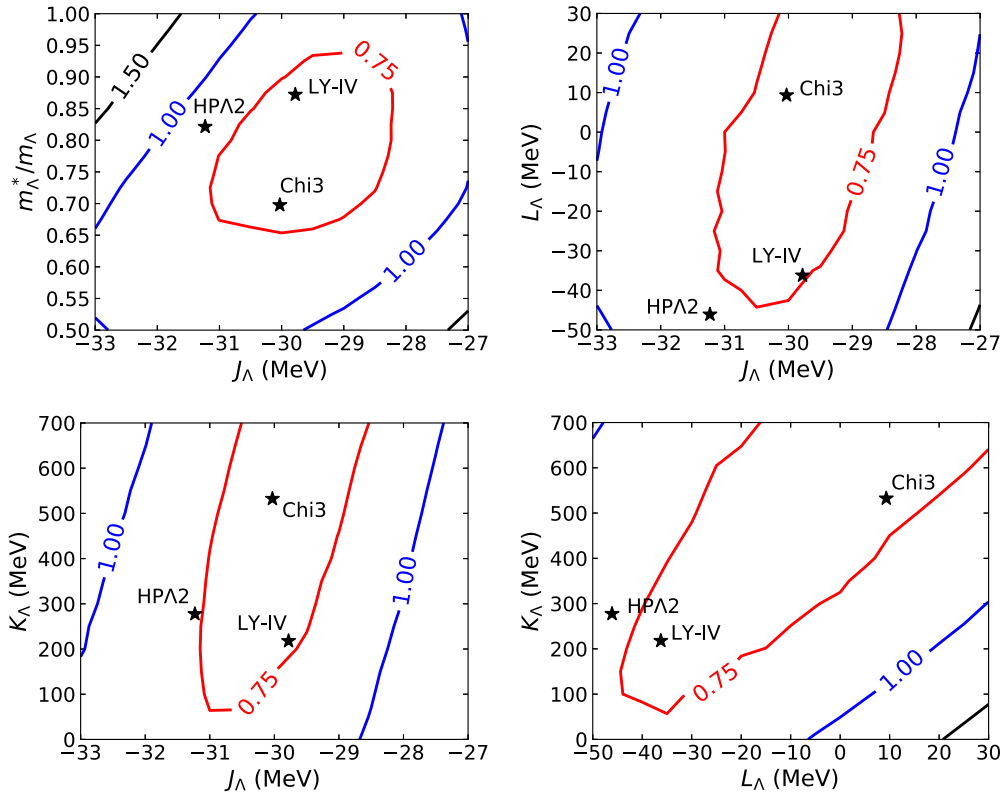

FIG. 6. Contour plot of the root-mean-square deviation ΔB_Λ of the calculated Λ binding energy from the experimental data. The stars indicate the points corresponding to the two parameters of Chi3, LY-IV, and HPΛ2. Note that the other parameters of those specific models do not necessarily match the optimized ones. Top left panel: ΔB_Λ as a function of the depth of the Λ potential at the saturation density, J_Λ, and the normalized effective mass m^*_Λ/m_Λ. The first and second derivatives, L_Λ and K_Λ, are optimized for minimizing ΔB_Λ for each point of $(J_\Lambda, m^*_\Lambda/m_\Lambda)$ by using the golden-section search. Top right panel: ΔB_Λ as a function of the depth of the Λ potential, J_Λ, and the first derivative L_Λ, where $(K_\Lambda, m^*_\Lambda/m_\Lambda)$ are optimized. Bottom left panel: ΔB_Λ as a function of the depth of Λ potential J_Λ and the second derivative K_Λ, where $(L_\Lambda, m^*_\Lambda/m_\Lambda)$ are optimized. Bottom right panel: ΔB_Λ as a function of the first derivative L_Λ and the second derivative K_Λ, where $(J_\Lambda, m^*_\Lambda/m_\Lambda)$ are optimized.

L_Λ make the potential deeper at $\rho < \rho_0$ while larger values of K_Λ make it shallower. Nevertheless, the uncertainty region with $\Delta B_\Lambda < 0.75$ MeV is not small enough, i.e., the sizes of the region are about 40 and 400 MeV for L_Λ and K_Λ, respectively. This reflects the fact that the Λ potential at $\rho < \rho_0$ is not sufficiently limited to discriminate Chi3 from LY-IV.

It should be noted that the ΔB_Λ values of the specific models (e.g., LY-IV) in Table. I do not necessarily match ΔB_Λ at their locations in Figs. 6 and 7. This is because the other parameters (i.e., optimized parameters and a_3^Λ) are different from the parameters in the specific model. The ΔB_Λ value depends on $(J_\Lambda, L_\Lambda, K_\Lambda, m^*_\Lambda/m_\Lambda, a_3^\Lambda)$, but only two of them are the same with the specific models in each panel of Figs. 6 and 7. For example, in the top left panel of Fig. 6, the other parameters $(K_\Lambda, L_\Lambda, a_3^\Lambda)$ are determined for each pair of $(J_\Lambda, m^*_\Lambda/m_\Lambda)$ so that they minimize ΔB_Λ while keeping the Λ binding energy of ${}^{13}_{\Lambda}$C, $B_\Lambda({}^{13}_{\Lambda}\mathrm{C})$. However, such a set of parameters does not necessarily match the parameters of the specific models, which are determined by different criteria. Specifically, we use the up-to-date value of $B_\Lambda({}^{13}_{\Lambda}\mathrm{C}) = 11.88$ MeV in our work to fix the value of a_3^Λ, while $B_\Lambda({}^{13}_{\Lambda}\mathrm{C}) = 11.69$ MeV is used in LY-IV [49]. It should also be noted that the ΔB_Λ value at the location of a specific model (e.g., LY-IV) differs for each panel because the optimized parameter sets at the LY-IV locations are different for different panels. Only two parameters are matched to LY-IV in each panel, and the combination of the two parameters differs for each panel.

We show ΔB_Λ for three different values of J_Λ as functions of L_Λ and K_Λ in Fig. 7, where the parameter m^*_Λ/m_Λ is optimized to minimize ΔB_Λ for each $(J_\Lambda, L_\Lambda, K_\Lambda)$ employing the golden-section search. For $J_\Lambda = -29$ MeV, we see that the parameter region of the Λ potentials with small ΔB_Λ have larger L_Λ and K_Λ compared to the case of unconstrained J_Λ (the bottom right panel of Fig. 6). This is because, to explain the Λ binding energy with a shallow potential, the Λ potential at $\rho \lesssim \rho_0$ has to be deeper by taking large L_Λ. For $J_\Lambda = -31$ MeV, the parameter region of $\Delta B_\Lambda < 0.78$ MeV has upper limits at $L_\Lambda = 0$ MeV and $K_\Lambda = 550$ MeV. In contrast to the case of $J_\Lambda = -29$ MeV, the Λ potential at $\rho \lesssim \rho_0$ has to be shallower by taking small L_Λ. Thus,

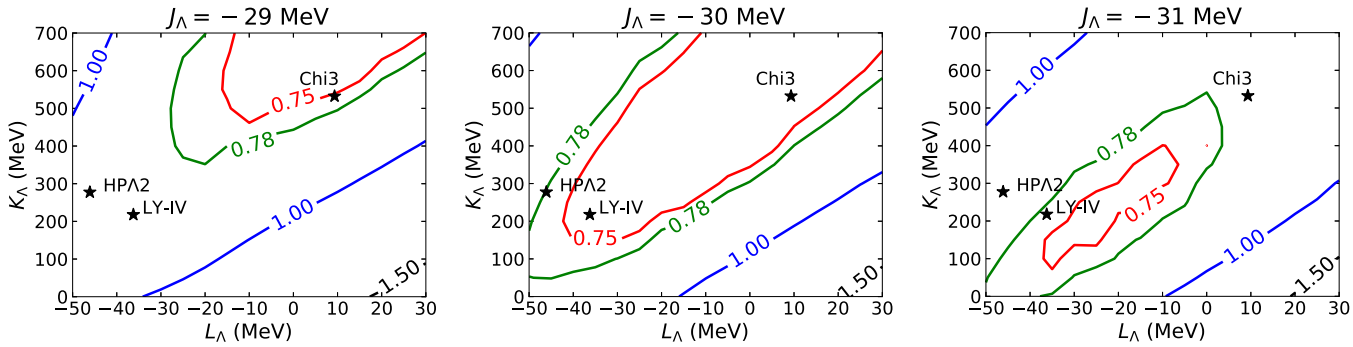

FIG. 7. Same as the bottom right panel of Fig. 6, but for three different fixed values of J_Λ. The normalized effective mass m^*_Λ/m_Λ is optimized for minimizing ΔB_Λ for each $(J_\Lambda, L_\Lambda, K_\Lambda)$ by using the golden-section search.

measuring J_Λ within the error of 1 MeV enables us to constrain the range of L_Λ and then K_Λ through the positive correlation. This helps to discuss whether the Λ potential is repulsive or attractive at high densities. For $J_\Lambda = -30$ MeV, the parameter region within $\Delta B_\Lambda < 0.75$ MeV includes various K_Λ values that are the same as those in the bottom right panel of Fig. 6. Therefore, if J_Λ is determined as −30 MeV by high-resolution data of the Λ binding energy, further constraint at $\rho < \rho_0$ is needed to determine L_Λ and K_Λ.

IV. Λ ADMIXTURE IN NEUTRON STAR MATTER

In the previous section, we examined the parameter space of Λ potentials consistent with the Λ binding energy data. In this section, we discuss the admixture of Λ in neutron stars by the chemical potentials and investigate the parameter region where Λ's do not appear in neutron stars. The Λ hyperons appear in neutron star matter at the baryon density ρ when the minimal chemical potential of Λ,

$$\mu^0_\Lambda(\rho) = m_\Lambda c^2 + U_\Lambda(\rho, k_\Lambda = 0), \tag{34}$$

exceeds the neutron chemical potential.

We determine the neutron chemical potential in neutron star ($npe\mu$) matter by solving the β-equilibrium conditions,

$$\mu_n = \mu_p + \mu_e, \tag{35}$$

$$\mu_e = \mu_\mu, \tag{36}$$

together with the baryon number conservation and the charge neutrality condition,

$$\rho = \rho_p + \rho_n, \tag{37}$$

$$\rho_p = \rho_e + \rho_\mu, \tag{38}$$

where

$$\mu_i = \left(\frac{\partial \tilde{\mathcal{E}}}{\partial \rho_i}\right)_{\rho_j \neq \rho_i}, \quad i, j = n, p, e, \mu, \tag{39}$$

are the chemical potentials of the matter constituents, and ρ_i $(i = n, p, e, \mu)$ are the corresponding densities. The total energy density $\tilde{\mathcal{E}}$ is given as

$$\tilde{\mathcal{E}}(\rho_n, \rho_p, \rho_e, \rho_\mu) = \tilde{\mathcal{E}}_N(\rho_n, \rho_p) + m_n c^2 \rho_n + m_p c^2 \rho_p + \tilde{\mathcal{E}}_e(\rho_e) + \tilde{\mathcal{E}}_\mu(\rho_\mu), \tag{40}$$

where $\tilde{\mathcal{E}}_N$ is the nucleon energy density and c is the speed of light. The energy densities of electrons $\tilde{\mathcal{E}}_e$ and muons $\tilde{\mathcal{E}}_\mu$ are assumed to be those of the Fermi gas. For the energy density of nucleons $\tilde{\mathcal{E}}_N$, we use the SLy4 [61] and BSk24 [72] parameter sets. Both are in good agreement with the pure neutron matter EOS from the χEFT up to the next-to-next-to-next-to-leading order (N3LO) [73,74]. SLy4 is a softer EOS with the maximum neutron star mass of $2.06 M_\odot$ compared to BSk24 with $2.28 M_\odot$.

In Fig. 8, we compare the minimal chemical potential of Λ, μ^0_Λ, and μ_n in the neutron star matter as a function of the normalized baryon density ρ/ρ_0. In the top panel, we confirm that the minimal Λ chemical potential of Chi3 is larger than the neutron chemical potential at $\rho/\rho_0 \leqslant 5$ as reported in Ref. [23]. On the other hand, by using the Λ potentials of LY-IV and HPΛ2, Λ hyperons are found to admix in neutron stars in the density range 2–3 ρ_0, as found in phenomenological models with hyperons [2–6], causing the softening of the EOS. In the bottom panel, all the Λ-potential models are found to exhibit the appearance of Λ's in neutron stars, representing that the appearance of Λ's depends on the model of the nucleonic EOS.

In Fig. 9, the minimal Λ chemical potentials calculated from the selected Λ potentials shown in Fig. 5 are compared with the neutron chemical potential in neutron star matter. The solid red lines correspond to the minimum Λ chemical potentials that suppress the appearance of Λ in neutron matter, i.e., $\mu^0_\Lambda > \mu_n$ at $\rho/\rho_0 \leqslant 5$. We confirmed that the suppression of Λ appearance hardly changes even when we check it up to the central density of a maximum-mass neutron star ($\rho \leqslant \rho_c^{\max}$) instead of $\rho/\rho_0 \leqslant 5$: the number of Λ potentials with no Λ appearance decreases only by two for SLy4 with $\rho_c^{\max} = 7.5\rho_0$ and is unchanged for BSk24 with $\rho_c^{\max} = 9.4\rho_0$, where $\rho_c^{\max}$ is taken from the CompOSE database [75] for each EOS. For $\rho > 3.5\rho_0$, the minimum Λ chemical potentials are split into 19 groups corresponding to $K_\Lambda = 100$, 150, 200, …, and 1000 MeV. We note that the gaps between the 19 groups

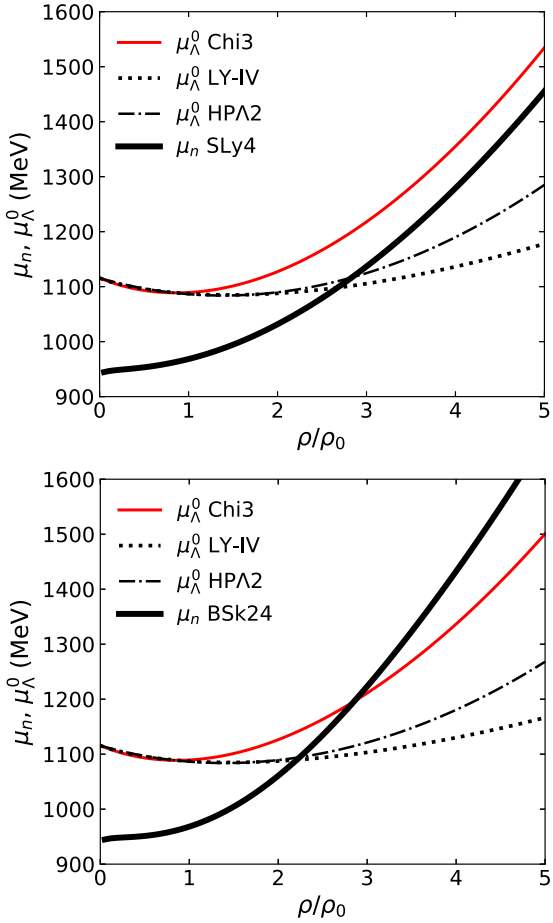

FIG. 8. Λ chemical potentials at zero momentum and neutron chemical potential in neutron star ($npe\mu$) matter are depicted as a function of the normalized baryon density. The solid, dotted, and dash-dotted lines correspond to the Λ chemical potential at zero momentum for Chi3, LY-IV, and HPΛ2, respectively. The bold solid line represents the neutron chemical potential calculated by using the SLy4 (upper panel) and BSk24 (lower panel) parameter sets.

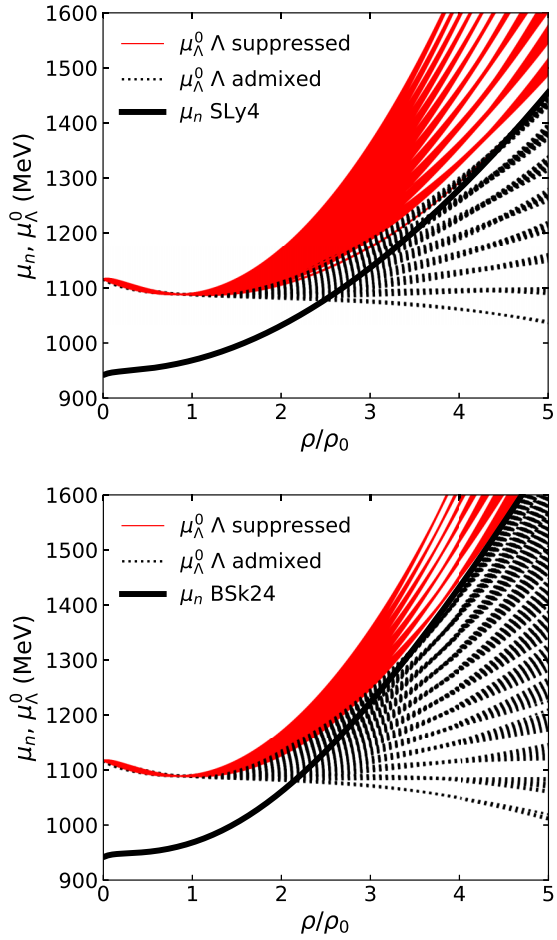

FIG. 9. Same as Fig. 8, but the Λ chemical potentials at zero momentum using the density dependence of the selected Λ potentials in Fig. 5 are shown. The solid red lines are the Λ potentials with $\mu_\Lambda^0 > \mu_n$ at $\rho/\rho_0 \leqslant 5$, which suppress the Λ hyperons in neutron star matter, while the dotted lines are those which fulfill the condition $\mu_\Lambda^0 \leqslant \mu_n$ at some densities so that Λ hyperons are admixed.

would be filled by considering more points in K_Λ. We also note that several parameter sets with different L_Λ's and J_Λ's are degenerate in each group, which means that the high-density part of the Λ chemical potential is mostly determined by K_Λ. We argue that the onset of Λ hyperons in neutron stars can be judged using the value of K_Λ: with the SLy4 EOS Λ's do not appear in neutron stars if $K_\Lambda \geqslant 500$ MeV, while with the BSk24 EOS Λ's do not appear if $K_\Lambda \geqslant 700$ MeV. Therefore, the second derivative of the Λ potential, K_Λ, would be the important parameter in discussing the admixture of Λ's in neutron star matter.

V. SUMMARY

We have examined the Λ potentials using the binding energies of Λ in hypernuclei within the Skyrme-Hartree-Fock method with spherical symmetry. It is found that the Λ potential from the χEFT [23,34] with two- and three-body force reproduces the experimental Λ binding energy data at the same level of accuracy as LY-IV [49] potential, while χEFT with only two-body force overestimates the Λ binding energy. Thus, the χEFT Λ potential which suppresses Λ in dense neutron star matter is consistent with the Λ binding energy. Taken together with our previous work [42], we conclude that the Λ-suppressed scenario is consistent with the Λ directed flow data of heavy-ion collisions and the Λ binding energy data of hypernuclei. More detailed studies are necessary in future work considering the YY and YYN interactions.

Next, we search for the parameter space of the Λ potentials by varying the Taylor coefficients and the effective mass at the saturation density. The root-mean-square deviation ΔB_Λ is used to evaluate the consistency between the calculated Λ binding energies and experimental data. It is shown that the depth of the Λ potential J_Λ is constrained from the Λ binding energy data within the accuracy of $-31.5 < J_\Lambda < -28$ MeV. These values are consistent with the well-known Woods-Saxon results [71]. There are lower and upper limits for the normalized effective mass: $0.65 < m_\Lambda^*/m_\Lambda < 0.95$.

TABLE II. SLy4 [61] parameter set.

Parameter	Value
t_0 (MeV fm^3)	−2488.91
t_1 (MeV fm^5)	486.82
t_2 (MeV fm^5)	−546.39
t_3 (MeV fm$^{3+3\gamma}$)	13777.0
x_0	0.834
x_1	−0.344
x_2	−1.000
x_3	1.354
γ	1/6
W_0 (MeV fm^5)	123.0

This reflects the fact that the energy splitting between orbitals is sensitive to the effective mass.

A positive correlation between the first- and second-order Taylor coefficients of the Λ potential, L_Λ and K_Λ, is found, which reflects the fact that the Λ potential at $\rho < \rho_0$ is constrained. It is shown that K_Λ can be well constrained by determining J_Λ within the accuracy of 1 MeV, i.e., $K_\Lambda > 350$ MeV is favored for $J_\Lambda = -29$ MeV, while $K_\Lambda < 550$ MeV is favored for $J_\Lambda = -31$ MeV. In the future, the value of J_Λ is expected to be determined more precisely through high-resolution data obtained at the Japan Proton Accelerator Research Complex (J-PARC) [76]. These data can be used to constrain the second-order Taylor coefficient K_Λ. Also, the Λ potentials with $K_\Lambda \geqslant 500$ MeV are found to suppress Λ's in β-stable neutron star matter for SLy4, while the Λ potentials with $K_\Lambda \geqslant 700$ MeV for BSk24 suppress Λ. Therefore, the determination of J_Λ helps discriminate the Λ-avoiding scenario from the Λ-admixing scenario in neutron stars.

To precisely determine the Λ potential at high densities, it would also be important to investigate other experimental data in future works. For example, the observables in heavy-ion collisions may be sensitive to the Λ potential at high densities: the elliptic flow including the centrality dependence and nuclear cluster production can be affected by the Λ potential. Also, the hypertriton ${}^3_\Lambda$H directed flow, which was recently measured by the STAR Collaboration [77], would be a promising future work. For another example, the value of K_Λ could be constrained by the excitation spectra of the breathing mode for Λ hypernuclei [78] in the same way as the incompressibility of nuclear matter, K. The Λ hypernuclei with large surface, such as neutron-rich hypernuclei, might also give constraints on the Λ potential.

ACKNOWLEDGMENTS

We thank Prof. Hirokazu Tamura for his useful comments and Prof. Kouichi Hagino for his careful reading of the manuscript and helpful comments. This work was supported in part by the Grants-in-Aid for Scientific Research from JSPS (Grants No. JP21K03577, No. JP19H01898, No. JP21H00121, and No. JP23K13102). This work was also supported by JST, the establishment of university fellowships towards the creation of science technology innovation, Grant No. JPMJFS2123.

APPENDIX A: EXPLICIT EXPRESSIONS OF THE SKYRME-HARTREE-FOCK POTENTIALS AND DENSITIES

Here, explicit forms of the terms appearing in the Skyrme-Hartree-Fock equation (12) are given as in Refs. [50,61]. The effective mass is defined by

$$\frac{\hbar^2}{2m_q^*} = \frac{\hbar^2}{2m_q} + \frac{1}{8}[t_1(2+x_1)t_2(2+x_2)]\rho_N + \frac{1}{8}[t_1(2x_1+1) - t_1(2x_1+1)]\rho_q + a_2^\Lambda \rho_\Lambda. \quad \text{(A1)}$$

The single-particle and spin-orbit potentials are given by

$$V_q = V_q^N + V_q^\Lambda + \delta_{q,p} V_{\rm coul}, \quad \text{(A2)}$$

$$W_q = \frac{1}{2}W_0 \frac{\mathrm{d}}{\mathrm{d}r}[\rho_N + \rho_q] - \frac{1}{8}(t_1 x_1 + t_2 x_2) J_N(r) + \frac{1}{8}(t_1 - t_2) J_q(r), \quad \text{(A3)}$$

TABLE III. Experimental data of Λ binding energy (B.E.) for various hypernuclei used in this work.

	B.E. (MeV)				
Hypernucleus	1s	1p	1d	1f	1g
${}^{16}_\Lambda$O [65]	12.92 ± 0.35	2.35 ± 0.05			
${}^{28}_\Lambda$Si [65]	17.1 ± 0.2	7.5 ± 0.2			
${}^{32}_\Lambda$S [79]	17.5 ± 0.5				
${}^{40}_\Lambda$Ca [80]	18.7 ± 1.1				
${}^{51}_\Lambda$V [65,81]	20.47 ± 0.13	11.77 ± 0.16	3.05 ± 0.13		
${}^{56}_\Lambda$Fe [79]	21.0 ± 1.0				
${}^{89}_\Lambda$Y [65]	23.6 ± 0.5	17.0 ± 1.0	9.6 ± 1.3	2.8 ± 1.2	
${}^{139}_\Lambda$La [65]	25.0 ± 1.2	20.9 ± 0.6	14.8 ± 0.6	8.5 ± 0.6	2.0 ± 0.6
${}^{208}_\Lambda$Pb [65]	26.8 ± 0.8	22.4 ± 0.6	17.3 ± 0.7	12.2 ± 0.6	7.1 ± 0.6

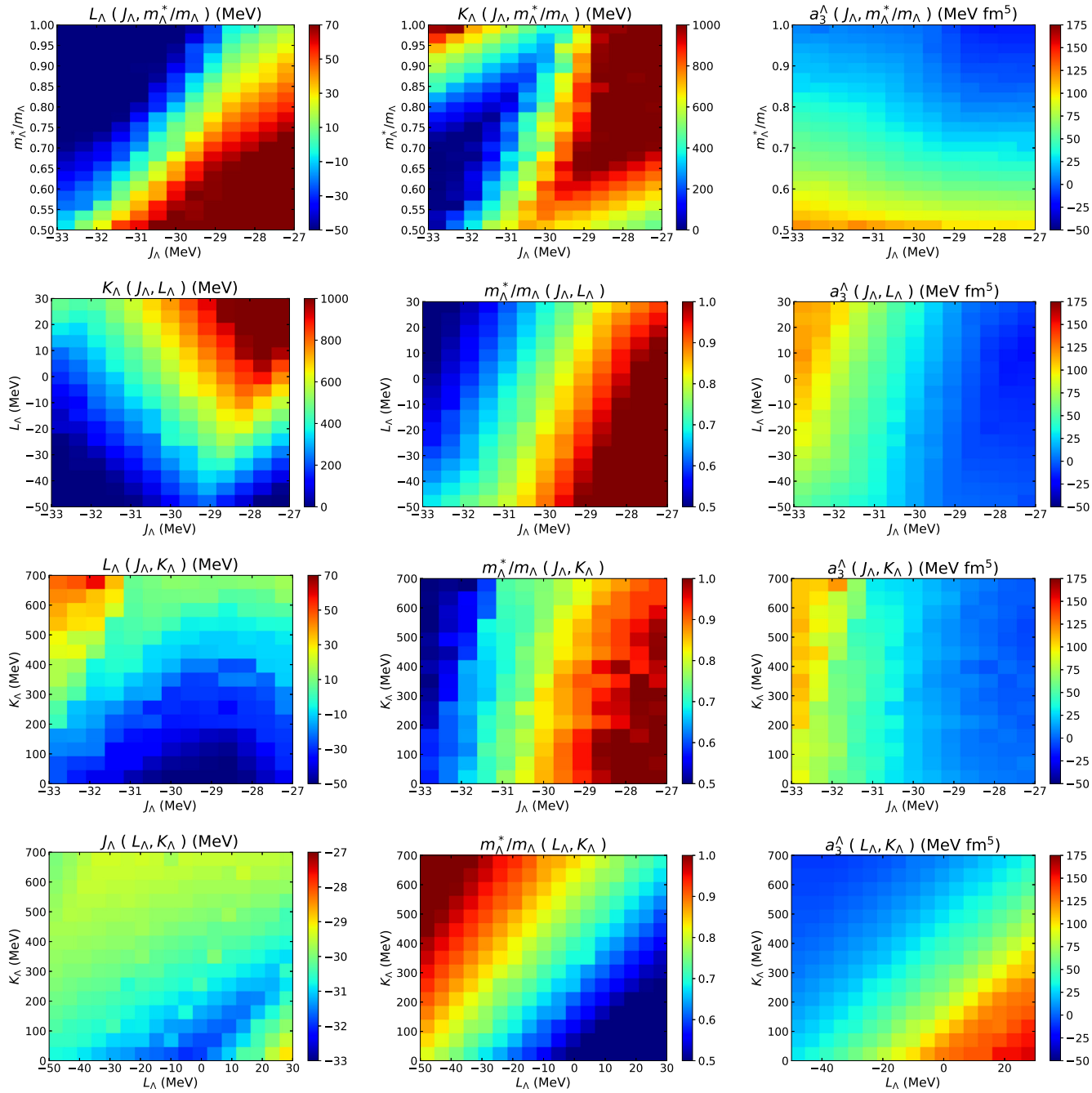

FIG. 10. Heat maps of the optimized parameters in Fig. 6. The parameters are optimized for minimizing ΔB_Λ at each grid point.

respectively, where

$$\begin{aligned} V_q^N = {} & \tfrac{1}{2}t_0(2+x_0)\rho_N + \tfrac{1}{2}t_0(2x_0+1)\rho_q \\ & + (\gamma+2)\tfrac{1}{24}t_3(2+x_3)\rho_N^{\gamma+1} \\ & + \tfrac{1}{24}t_3(2x_3+1)\left[\gamma\rho_N^{\gamma-1}\left(\rho_p^2+\rho_n^2\right)+2\rho_N^\gamma\rho_q\right] \\ & + \tfrac{1}{8}\left[t_1(2+x_1)t_2(2+x_2)\right]\tau_N \\ & + \tfrac{1}{8}[t_1(2x_1+1)-t_1(2x_1+1)]\tau_q \\ & - \tfrac{1}{16}[3t_1(2+x_1)-t_2(2+x_2)]\Delta\rho_N \\ & - \tfrac{1}{16}[3t_1(2x_1+1)+t_2(2x_2+1)]\Delta\rho_q \\ & - \tfrac{1}{2}W_0[\nabla\cdot\boldsymbol{J}_N+\nabla\cdot\boldsymbol{J}_q], \end{aligned} \tag{A4}$$

$$\begin{aligned} V_q^\Lambda = {} & a_1^\Lambda\rho_\Lambda + a_2^\Lambda\tau_\Lambda - a_3^\Lambda\Delta\rho_\Lambda \\ & + (1+\gamma_1)a_4^\Lambda\rho_N{}^{\gamma_1}\rho_\Lambda + (1+\gamma_2)a_5^\Lambda\rho_N{}^{\gamma_2}\rho_\Lambda, \end{aligned} \tag{A5}$$

$$V_{\rm coul} = e^2\int \mathrm{d}^3r'\,\frac{\rho_p(\boldsymbol{r}')}{|\boldsymbol{r}-\boldsymbol{r}'|} - e^2\left(\frac{3\rho_p}{\pi}\right)^{1/3}. \tag{A6}$$

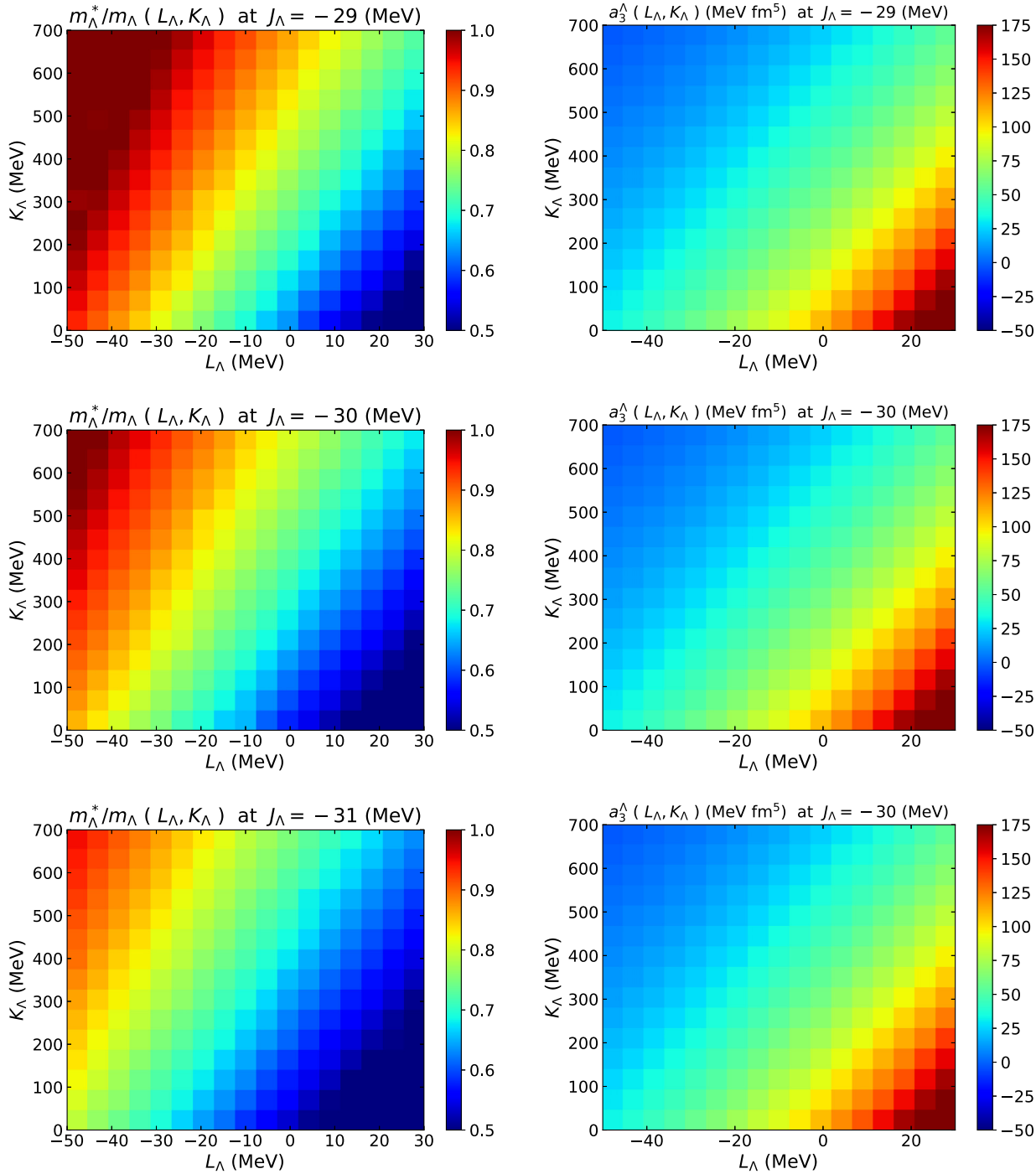

FIG. 11. Heat maps of the optimized parameters in Fig. 7.

The values of the parameters t_i, x_i, γ, and W_0 are given by the SLy4 parameter set shown in Table II. The isospins $q = \pm 1/2$ specify the neutron and proton, respectively. The density ρ_q and the kinetic density τ_q are given by Eq. (8) while the spin density $\boldsymbol{J}_q$ is written as

$$\boldsymbol{J}_q(\boldsymbol{r}) = -i \sum_i \phi_i^*(\boldsymbol{r}, q) \nabla \phi_i(\boldsymbol{r}, q) \times \langle \sigma' | \boldsymbol{\sigma} | \sigma \rangle. \tag{A7}$$

The nucleon density, the kinetic density, and the spin density are defined as $\rho_N = \sum_q \rho_q$, $\tau_N = \sum_q \tau_q$, and $\boldsymbol{J}_N = \sum_q \boldsymbol{J}_q$, respectively.

APPENDIX B: Λ BINDING ENERGY DATA

The Λ binding energy data used in this study are summarized in Table III. The data measured in the (π^+, K^+) experiments listed in Ref. [65] ($^{16}_{\Lambda}$O, $^{28}_{\Lambda}$Si, $^{51}_{\Lambda}$V, $^{139}_{\Lambda}$La, $^{208}_{\Lambda}$Pb) are used with the modification 0.5 MeV as pointed out in Ref. [66].

APPENDIX C: OPTIMIZED PARAMETERS

The optimized parameters in Figs. 6 and 7 are summarized in Figs. 10 and 11, respectively. Those parameters are optimized for minimizing ΔB_Λ for each grid point.

[1] G. Baym, T. Hatsuda, T. Kojo, P. D. Powell, Y. Song, and T. Takatsuka, Rep. Prog. Phys. **81**, 056902 (2018).
[2] N. K. Glendenning and S. A. Moszkowski, Phys. Rev. Lett. **67**, 2414 (1991).
[3] J. Schaffner and I. N. Mishustin, Phys. Rev. C **53**, 1416 (1996).
[4] S. Balberg and A. Gal, Nucl. Phys. A **625**, 435 (1997).
[5] M. Baldo, G. F. Burgio, and H. J. Schulze, Phys. Rev. C **61**, 055801 (2000).
[6] I. Vidana, A. Polls, A. Ramos, L. Engvik, and M. Hjorth-Jensen, Phys. Rev. C **62**, 035801 (2000).
[7] M. Fortin, S. S. Avancini, C. Providência, and I. Vidaña, Phys. Rev. C **95**, 065803 (2017).
[8] F. Özel, D. Psaltis, S. Ransom, P. Demorest, and M. Alford, Astrophys. J. **724**, L199 (2010).
[9] S. Weissenborn, I. Sagert, G. Pagliara, M. Hempel, and J. Schaffner-Bielich, Astrophys. J. **740**, L14 (2011).
[10] L. Bonanno and A. Sedrakian, Astron. Astrophys. **539**, A16 (2012).
[11] T. Klähn, R. Łastowiecki, and D. B. Blaschke, Phys. Rev. D **88**, 085001 (2013).
[12] E. Annala, T. Gorda, A. Kurkela, J. Nättilä, and A. Vuorinen, Nat. Phys. **16**, 907 (2020).
[13] T. Kojo, G. Baym, and T. Hatsuda, Astrophys. J. **934**, 46 (2022).
[14] H. Dapo, B.-J. Schaefer, and J. Wambach, Phys. Rev. C **81**, 035803 (2010).
[15] S. Nishizaki, T. Takatsuka, and Y. Yamamoto, Prog. Theor. Phys. **108**, 703 (2002).
[16] P. Demorest, T. Pennucci, S. Ransom, M. Roberts, and J. Hessels, Nature (London) **467**, 1081 (2010).
[17] J. Antoniadis *et al.*, Science **340**, 1233232 (2013).
[18] E. Fonseca *et al.*, Astrophys. J. **832**, 167 (2016).
[19] H. T. Cromartie *et al.* (NANOGrav Collaboration), Nat. Astron. **4**, 72 (2019).
[20] M. C. Miller *et al.*, Astrophys. J. Lett. **918**, L28 (2021).
[21] D. Lonardoni, A. Lovato, S. Gandolfi, and F. Pederiva, Phys. Rev. Lett. **114**, 092301 (2015).
[22] M. M. Nagels, T. A. Rijken, and Y. Yamamoto, Phys. Rev. C **99**, 044003 (2019).
[23] D. Gerstung, N. Kaiser, and W. Weise, Eur. Phys. J. A **56**, 175 (2020).
[24] Y. Yamamoto, T. Furumoto, N. Yasutake, and T. A. Rijken, Phys. Rev. C **88**, 022801(R) (2013).
[25] Y. Yamamoto, T. Furumoto, N. Yasutake, and T. A. Rijken, Phys. Rev. C **90**, 045805 (2014).
[26] Y. Yamamoto, T. Furumoto, N. Yasutake, and T. A. Rijken, Eur. Phys. J. A **52**, 19 (2016).
[27] H. Togashi, E. Hiyama, Y. Yamamoto, and M. Takano, Phys. Rev. C **93**, 035808 (2016).
[28] J. Haidenbauer, U. G. Meißner, N. Kaiser, and W. Weise, Eur. Phys. J. A **53**, 121 (2017).
[29] D. Logoteta, I. Vidana, and I. Bombaci, Eur. Phys. J. A **55**, 207 (2019).
[30] S. Choi, E. Hiyama, C. H. Hyun, and M.-K. Cheoun, Eur. Phys. J. A **58**, 161 (2022).
[31] S. Weissenborn, D. Chatterjee, and J. Schaffner-Bielich, Phys. Rev. C **85**, 065802 (2012) [**90**, 019904(E) (2014)].
[32] D. Chatterjee and I. Vidaña, Eur. Phys. J. A **52**, 29 (2016).
[33] E. Epelbaum, H.-W. Hammer, and U.-G. Meissner, Rev. Mod. Phys. **81**, 1773 (2009).
[34] M. Kohno, Phys. Rev. C **97**, 035206 (2018).
[35] S. Petschauer, J. Haidenbauer, N. Kaiser, U.-G. Meißner, and W. Weise, Nucl. Phys. A **957**, 347 (2017).
[36] Y. Akiba *et al.*, arXiv:1502.02730.
[37] M. Arslandok *et al.*, arXiv:2303.17254.
[38] X. Luo, Nucl. Phys. A **956**, 75 (2016).
[39] N. Abgrall *et al.* (NA61 Collaboration), J. Instrum. **9**, P06005 (2014).
[40] P. Danielewicz, R. Lacey, and W. G. Lynch, Science **298**, 1592 (2002).
[41] Y. Nara and A. Ohnishi, Phys. Rev. C **105**, 014911 (2022).
[42] Y. Nara, A. Jinno, K. Murase, and A. Ohnishi, Phys. Rev. C **106**, 044902 (2022).
[43] Y. Nara, JAM2, https://gitlab.com/transportmodel/jam2.
[44] L. Adamczyk *et al.* (STAR Collaboration), Phys. Rev. Lett. **120**, 062301 (2018).
[45] J. Adam *et al.* (STAR Collaboration), Phys. Rev. C **103**, 034908 (2021).
[46] M. S. Abdallah *et al.* (STAR Collaboration), Phys. Lett. B **827**, 137003 (2022).
[47] D. J. Millener, C. B. Dover, and A. Gal, Phys. Rev. C **38**, 2700 (1988).
[48] Y. Yamamoto, H. Bando, and J. Zofka, Prog. Theor. Phys. **80**, 757 (1988).
[49] D. E. Lanskoy and Y. Yamamoto, Phys. Rev. C **55**, 2330 (1997).
[50] N. Guleria, S. K. Dhiman, and R. Shyam, Nucl. Phys. A **886**, 71 (2012).
[51] J. Haidenbauer and I. Vidana, Eur. Phys. J. A **56**, 55 (2020).
[52] J. Haidenbauer, S. Petschauer, N. Kaiser, U. G. Meissner, A. Nogga, and W. Weise, Nucl. Phys. A **915**, 24 (2013).
[53] J. Haidenbauer, U. G. Meißner, and A. Nogga, Eur. Phys. J. A **56**, 91 (2020).
[54] M. Rayet, Ann. Phys. (NY) **102**, 226 (1976).
[55] M. Rayet, Nucl. Phys. A **367**, 381 (1981).
[56] P. B. Fernandez, E. G. Adelberger, and A. Garcia, Phys. Rev. C **40**, 1887 (1989).
[57] M. T. Win, K. Hagino, and T. Koike, Phys. Rev. C **83**, 014301 (2011).
[58] M. T. Win and K. Hagino, Phys. Rev. C **78**, 054311 (2008).
[59] K. Tsubakihara, H. Maekawa, H. Matsumiya, and A. Ohnishi, Phys. Rev. C **81**, 065206 (2010).
[60] Y. Tanimura and K. Hagino, Phys. Rev. C **85**, 014306 (2012).
[61] E. Chabanat, P. Bonche, P. Haensel, J. Meyer, and R. Schaeffer, Nucl. Phys. A **635**, 231 (1998) [**643**, 441(E) (1998)].
[62] S. Ajimura *et al.*, Phys. Rev. Lett. **86**, 4255 (2001).

[63] H. Akikawa *et al.*, Phys. Rev. Lett. **88**, 082501 (2002).
[64] S. Perez-Martin and L. M. Robledo, Phys. Rev. C **78**, 014304 (2008).
[65] O. Hashimoto and H. Tamura, Prog. Part. Nucl. Phys. **57**, 564 (2006).
[66] T. Gogami *et al.*, Phys. Rev. C **93**, 034314 (2016).
[67] E. Friedman and A. Gal, Phys. Lett. B **837**, 137669 (2023).
[68] E. Friedman and A. Gal, Nucl. Phys. A **1039**, 122725 (2023).
[69] I. Tews, J. M. Lattimer, A. Ohnishi, and E. E. Kolomeitsev, Astrophys. J. **848**, 105 (2017).
[70] J. Kiefer, Proc. Am. Math. Soc. **4**, 502 (1953).
[71] A. Gal, E. V. Hungerford, and D. J. Millener, Rev. Mod. Phys. **88**, 035004 (2016).
[72] S. Goriely, N. Chamel, and J. M. Pearson, Phys. Rev. C **88**, 024308 (2013).
[73] C. Drischler, R. J. Furnstahl, J. A. Melendez, and D. R. Phillips, Phys. Rev. Lett. **125**, 202702 (2020).
[74] G. F. Burgio, H. J. Schulze, I. Vidana, and J. B. Wei, Prog. Part. Nucl. Phys. **120**, 103879 (2021).
[75] S. Typel, M. Oertel, and T. Klähn, Phys. Part. Nuclei **46**, 633 (2015); M. Oertel, M. Hempel, T. Klähn, and S. Typel, Rev. Mod. Phys. **89**, 015007 (2017); S. Typel *et al.* (CompOSE Core Team), Eur. Phys. J. A **58**, 221 (2022).
[76] K. Aoki *et al.*, arXiv:2110.04462.
[77] B. E. Aboona *et al.* (STAR Collaboration), Phys. Rev. Lett. **130**, 212301 (2023).
[78] H. Tamura (private communication).
[79] H. Bando, T. Motoba, and J. Zofka, Int. J. Mod. Phys. A **05**, 4021 (1990).
[80] P. H. Pile *et al.*, Phys. Rev. Lett. **66**, 2585 (1991).
[81] H. Hotchi *et al.*, Phys. Rev. C **64**, 044302 (2001).